Gas phase Raman spectroscopy of non-reacting flows : comparison between free space and cavity based spontaneous Raman emission

LEE WELLER,[1,2,*] MAXIM KUVSHINOV,[1,2] AND SIMONE HOCHGREB[1]

[1]*Department of Engineering, University of Cambridge, Trumpington Street, Cambridge, CB2 1PZ, UK*
[2]*These authors contributed equally*
[*]*lw493@cam.ac.uk*

Abstract: We report on a comparison of free space and Cavity-Enhanced Raman Spectroscopy (CERS) for gas phase measurements of nitrogen and oxygen in ambient air. Real time analysis capabilities, and continuous Raman signals with low power diodes, make the technique non-invasive, affordable, compact and applicable for usage in non-reacting flows. We derive a comprehensive model for estimation of photon emission for both free space and cavity based signals and discuss trade-offs in how to organize the cavity geometry for maximum gain relative to free space. Measurements in both free and cavity configurations are compared to the expected signals, demonstrating the usefulness of the model in predicting amplification. The present results can serve as a quick guide on how to use low power continuous wave lasers in a cavity setup to obtain enhanced laser induced spontaneous Raman scattering.

1. Introduction

Laser induced Raman spectroscopy has become a widespread tool for the chemical analysis of condensed phase materials [1–5] relying on molecular vibrations to fingerprint bonds and species. However, its relatively low signal compared to elastic scattering and fluorescence means that it has not yet found general application for gas-phase species detection [6, 7] , with a few exceptions [8, 9]. Well known features of Raman spectroscopy include the ability to identify multiple species at a time (including homo-nuclear diatomic species), its insensitivity to the presence of water vapour, and the obtainment of instantaneous point-wise rather than line-of-sight measurements. Raman spectroscopy does not require a particular wavelength for the pump laser, however its signal is weaker in comparison to other spectroscopy techniques [6, 7]. Therefore making use of signal enhancement techniques and/or high pulse energies are essential, particularly where radiative or fluorescing backgrounds are significant. The use of multi-pass cavities, resonant or near-resonant excitation, and plasmonic enhancement (Surface Enhanced Raman Scattering (SERS)) can improve the signal sensitivity [10]. Under appropriate conditions, gas-phase Raman spectroscopy allows for fast measurements (sub-μs) at high repetition rates (up to several kHz) [11, 12]. High temporal resolution can be achieved (i.e. in unsteady flows) with nanosecond pulsed laser sources. On the other hand, in order to generate enough photons for Raman spectroscopy, high power laser sources are often required. Even though a number of techniques (polarization-resolved detection Raman, near-infrared Raman, shifted-excitation Raman difference spectroscopy (SERDS) and deep-UV Raman) have been developed to reduce interference from laser-induced fluorescence, it still remains a significant problem in many applications. Interference from elastically scattered light (i.e. Rayleigh scattering) can be orders of magnitude stronger than the anti-Stokes and Stokes signals [13]. Overcoming such difficulties requires large numerical apertures and signal filtering, which can be difficult to engineer.

[1]Accepted for publication in *Applied Optics*, 6 March 2019.

Spontaneous Raman scattering has found applications in many different fields of research and industry, including chemical kinetics of reacting flows, atmospheric sensing, surface chemistry, catalysis and biological and environmental processes. In chemical kinetics, vibrational spectroscopy has found use for Raman flame measurements in combustion [14–16] and Thomson scattering measurements of low-density plasmas [17]. Raman scattering allows detection of simple homoatomic gas species such as oxygen, nitrogen and hydrogen, including the isotopic tritium, providing a powerful method for quantitative gas-phase analysis and trace gas detection for environmental monitoring [18–20]. Studies of surface chemistry and catalysis using Raman spectroscopy include refining the theoretical analysis of molecular energy levels and potential energy hyper-surfaces [21], as well as improving the understanding of vibrational interactions and intramolecular vibrational energy redistribution [22, 23]. Biological and environmental studies include discrimination of isotopic labeled substrates, using the respiration quotient for metabolic studies [24], analyzing the rate of leakage of incubation chambers using sulfur hexafluoride [25], studies on biogas processes [26], on-site measurements of soil gases [27], quantification of denitrification and nitrogen fixation [28].

The main disadvantage of Raman detection for gases is its low signal magnitude due to low molecular densities: this requires high laser powers, making the experimental setups large and costly. However, a number of different approaches have been proposed to enhance the signal such as confining light in a fiber (Fiber Enhanced Raman Spectroscopy (FERS)) or amplifying the signal by using a resonant mirrored cavity. Cavity Enhanced Raman Spectroscopy (CERS) uses the ability of mirrored cavities to enhance the input power, by tuning the cavity to particular modes of the input laser wavelength [29, 30]. The approach takes advantage of the availability of affordable mirrors with high reflectivity surfaces, controllable mirror support bases, and inexpensive detection capabilities using low cost detectors or arrays. Further developments in CERS could allow real time, low cost, small footprint in situ measurements in a broad scope of scientific and industrial fields, ranging from the very small scale to planetary atmospheric detection, including biological analysis [31], fermentation gases [32], power plants [8], food quality control [33], and deep-sea explorations [34].

There have been numerous practical applications of CERS for chemical species detection. Taylor *et. al.* [35] stabilized a 1 W, 532 nm laser using a short, linear cavity via an electronic feedback mechanism and managed to observe Raman signals from hydrogen in a 90° collection geometry. A Raman cell was placed inside the optical cavity, but the windows of the cell introduced significant optical losses, limiting the enhancement factor to 50. Ohara *et. al.* [36] used an anti-reflection coated laser diode coupled into a linear optical cavity, while achieving an intracavity build-up of 800. They introduced a solid angle efficiency factor to quantify the collected Stokes photons for a 90° collection geometry from the middle of the cavity. Li *et. al.* [37] demonstrated a different configuration, creating a multi-pass cell in a near confocal cavity. This allowed a pump power build-up of 9 W from a 200 mW laser as the beam was reflected 50 times inside the cavity. Using CERS it was possible to carry out high-sensitivity detection of a mixture of eight gases, however the experimental set-up did not act as a resonant optical cavity. More recently, Hippler *et. al.* [29] demonstrated the capabilities of CERS by coupling a 635 nm laser diode into a linear optical external cavity, consisting of two highly reflective mirrors. A build-up of the circulating power of nearly three orders of magnitude (833) was achieved using optical feedback stabilization, with strong Raman signals collected in a forward scattering geometry. CERS spectra of air, CH_4, H_2 and benzene were recorded to demonstrate the capabilities for analytical applications and studies of fundamental molecules. Thorstensen *et. al.* [30] constructed a low-cost CERS probe for multi-gas detection. A 532 nm laser pointer was coupled into a Fabry-Perot cavity which allowed an increase in the sensitivity of the gas probe by a factor of 50. The use of inexpensive key experimental components such as mirrors, laser sources and detectors showed the possibility of CERS to be used as a low entry barrier analysis

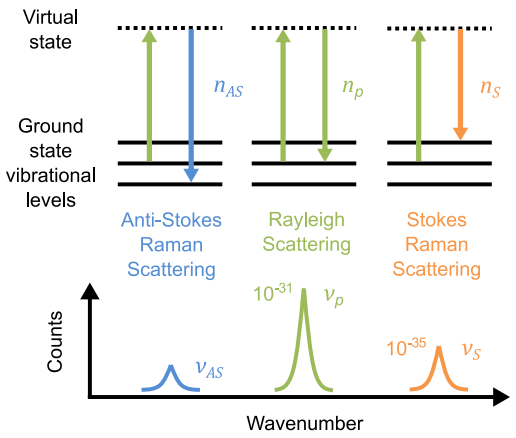

Fig. 1. Typical competing scattering processes and magnitude within an excited molecule.

technique. Friss *et. al.* [38] also demonstrated the ability of CERS in acquisition of the Raman spectra of air. A narrow linewidth fibre laser at 1064 nm was locked to a high-finesse cavity containing the sample gas. They managed to generate an intracavity power build-up from 3.7 mW to 22 W, resulting in a build-up factor of 5900. Rotational Raman and Rayleigh scattering data were collected for O_2, N_2 and CO_2. In the studies outlined above, a standardized figure of merit (FOM) is represented by the power amplification within the cavities, which is proportional to the finesse. In addition there were no comprehensive models describing the expected Stokes signal for 90° collection from the middle of the cavity or forward scattering geometries. The goal of this work is to compare the expected and experimental signals obtained from the use of an unconfined and confined continuous wave laser for excitation of a region of space for open path, *in situ* applications.

In this work we present the non-dimensional theoretical underpinnings for the expected Stokes Raman signal for a two-state free space and cavity model. The paper first presents the process of generating Stokes signals for laser-induced spontaneous Raman scattering in free space. This is then followed by a discussion of the geometric and optical conditions required for efficient resonant cavity enhancement, via a cavity setup. The FOM in previous CERS studies was the power amplification and resonant recirculation within the cavity. In this work we also incorporate the Purcell effect and discuss the need to satisfy the double resonance condition. Finally, we demonstrate the Raman signatures of common gas phase molecules (oxygen and nitrogen) obtained by the outlined techniques, and discuss the origins of the discrepancies between the expected and measured values, further highlighting the importance of the model controlling parameters.

2. Spontaneous Raman Scattering

2.1. Differential Raman scattering cross section

Laser-induced spontaneous Raman scattering is the inelastic scattering of an incident photon by a molecule in either the ground or higher rovibronic state. The incident photon causes a vibration or rotation within the molecule and the change in energy between the initial and final rovibronic states manifests itself in the difference between the scattered and incident photon wavelengths. Depending whether the final state is at higher or lower energy than the initial state, the shift in wavelength of the scattered photon is called Stokes or anti-Stokes, respectively. This shift in

Table 1. Raman scattering parameters and cross section for O_2 and N_2 using Eq. 3.

Molecule	Shift (cm^{-1})	A ($\times 10^{-32}$) m^2 sr^{-1}	ν_i ($\times 10^{15}$) Hz	$\frac{d\sigma}{d\Omega}$ ($\times 10^{-35}$) m^2 sr^{-1}
O_2	1555	0.459 [41]	1.71 [41]	4.88 [40]
N_2	2331	3.02 [41]	2.69 [41]	3.79 [40]

energy is known as the energy Raman shift, given by:

$$E_{S/AS} = h(\nu_p - \nu_{S/AS}) = hc(\tilde{\nu}_p - \tilde{\nu}_{S/AS}), \tag{1}$$

where h is Planck's constant, c is the speed of light, ν_p and $\nu_{S/AS}$ are the pump and Stokes/Anti-Stokes emission frequencies, and $\tilde{\nu}_p$ and $\tilde{\nu}_{S/AS}$ are the pump and Stokes/Anti-Stokes emission wavenumbers. When the scattered photon is emitted at the same energy as the incident photon, this is known as Rayleigh or elastic scattering. Rayleigh scattering intensities exceed those of Raman scattering by several orders of magnitude [39]). The Stokes (higher frequency and energy) signal is usually larger than the anti-Stokes signal due to the thermal distribution of energy states. Figure 1 shows an energy diagram for the typical Raman scattering processes and their relative magnitudes as a function of wavenumber. For the remainder of this paper we only consider the integrated vibrational Stokes signal.

For laser induced spontaneous Raman scattering, linearly polarized incident pump photons induce generation of unpolarized emitted Stokes photons in proportion to the number of incident photons and the differential cross section of the particular species. The differential Raman scattering cross section (area per unit collection solid angle) for a particular species can be approximated by (Eq. 5.10.1 in [5]):

$$\frac{d\sigma}{d\Omega} = \left(\frac{\alpha\pi}{\epsilon_0 c^2}\right)^2 \nu_S^4, \tag{2}$$

where ϵ_0 is the permittivity of free space and α is a general transition polarizability for the species. Experimentally measured values of α obtained from the anti-Stokes branch in the vibrational-rotational Raman spectrum of nitrogen (N_2) are around 5×10^{-42} C m^2 V^{-1} [5]. The differential Raman scattering cross section for 532 nm excitation wavelength ($\nu_p = 5.64 \times 10^{14}$ Hz) of the N_2 vibrational mode ($\nu_S = 4.94 \times 10^{14}$ Hz) at room temperature ($T = 293.15$ K) is 2.31×10^{-35} m^2 sr^{-1}. Previous work [40, 41] has measured the differential Raman scattering cross section of N_2 to be 3.79×10^{-35} m^2 sr^{-1} which is larger than the predicted value from Eq. 2. The same authors fitted Eq. 3 to the wavelength dependent differential Raman scattering cross sections in the form

$$\frac{d\sigma}{d\Omega} = A\left(\frac{\nu_S^2}{\nu_i^2 - \nu_p^2}\right)^2, \tag{3}$$

where A and ν_i are fitting parameters. For the reminder of this work we use Eq. 3 to calculate values of the differential Raman scattering cross section as a function of pump wavelength.

Table 1 shows parameters for the two species of interest (O_2 and N_2), including the fitting parameters for Eq. 3. The cross section values were calculated for 532 nm at room temperature (T = 293.15 K) and atmospheric pressure (101325 Pa). The values are four orders of magnitude smaller than the respective Rayleigh cross sections (O_2 = 4.74×10^{-31} m^2 sr^{-1} and N_2 = 5.30×10^{-31} m^2 sr^{-1} [39]). Therefore, in order to measure a quantifiable number of Stokes photons, one would need either a high power laser and/or a large number density. Next we consider the nondimensional parameters involved in a free space model.

2.2. Free space model

A detailed calculation of the rate of emission of Stokes photons can be found in [42,43]. The rate of change of the scattered free space Stokes photons can be given as a balance of the pump and Stokes processes between the ground and virtual states:

$$\frac{\mathrm{d}n_S}{\mathrm{d}t} = \frac{C_f}{\tau_0} n_p - \frac{1}{\tau_0} n_S \,, \tag{4}$$

where n_S is the number of scattered Stokes photons, n_p is the number of pump photons, C_f is a multiplier constant, and τ_0 is the lifetime of the free space Stokes photons. The latter is given by:

$$\frac{1}{\tau_0} = \frac{8\pi c}{3} \frac{\lambda_S}{\lambda_p} N \frac{\mathrm{d}\sigma}{\mathrm{d}\Omega} \,, \tag{5}$$

where c is the speed of light, N is the number of particles per unit volume, λ_p and λ_S are the pump and Stokes wavelengths and $\mathrm{d}\sigma/\mathrm{d}\Omega$ is the differential Raman scattering cross section (see Eq. 3 in Section 2.1). The free space factor, C_f, is given by

$$C_f = \frac{3}{8\pi^2} \left(\frac{\lambda_S}{n}\right)^3 \frac{1}{V_{\mathrm{eff}}^{(f)}} \frac{\nu_S}{\Delta\nu_S^{(f)}} \,, \tag{6}$$

where n is the index of refraction and $\Delta\nu_S^{(f)}$ is the free space Stokes line-width. The effective volume, which assumes a perfect overlap of the Gaussian beam waist with the collection solid angle, that are perpendicular to each other, is given by [44]:

$$V_{\mathrm{eff}}^{(f)} = \frac{128}{3\pi^2} \frac{f^3 \lambda_p^3}{d^3} \,. \tag{7}$$

where d is the diameter at the lens and f is the focal length, as can be seen in Figure 2. Substituting Eqs. 5, 6 and 7 into Eq. 4 gives the rate equation:

$$\frac{\mathrm{d}n_s}{\mathrm{d}t} = \left(\frac{3\pi c}{128} \frac{Nd^3}{n^3 f^3} \frac{\nu_p^4}{\nu_S^3 \Delta\nu_S^{(f)}} \frac{\mathrm{d}\sigma}{\mathrm{d}\Omega}\right) n_p - \frac{n_S}{\tau_0} \,. \tag{8}$$

Assuming a steady state solution ($\mathrm{d}n_s/\mathrm{d}t = 0$), the rate of emission of Stokes photons collected ($\gamma_f = n_S/\tau_0$) is equal to the rate of pumped photons:

$$\gamma_f = \left(\frac{3\pi c}{128} \frac{Nd^3}{n^3 f^3} \frac{\nu_p^4}{\nu_S^3 \Delta\nu_S^{(f)}} \frac{\mathrm{d}\sigma}{\mathrm{d}\Omega}\right) n_p \,. \tag{9}$$

One can now express the rate of Stokes photons emitted as a function of the pump power by assuming that the power is uniformly distributed over its line width, $n_p = 2P_{\mathrm{in}}\tau_p^{(f)}/h\nu_p$ where P_{in} is the pump input power and $\tau_p^{(f)} = 1/(2\pi\Delta\nu_p^{(f)})$, where $\Delta\nu_p^{(f)}$ is the free space pump line-width. The expression for the rate of laser-induced Stokes photon emission from a CW laser becomes:

$$\gamma_f = \frac{3c}{128} \frac{Nd^3 P_{\mathrm{in}}}{n^3 f^3 h} \frac{\mathrm{d}\sigma}{\mathrm{d}\Omega} \frac{\nu_p^3}{\nu_S^3} \frac{1}{\Delta\nu_S^{(f)} \Delta\nu_p^{(f)}} \,. \tag{10}$$

which shows that the Raman signal is a strong function of the line-widths of the pump laser (which is governed by the type of laser) and the Stokes line-width, which depends on the species of

interest. Now we nondimensionalize Eq. 10 to gain further insight into the parameters controlling the Stokes emission rate:

$$\gamma_f = \left(\frac{3\mathrm{NA}^3}{16n^3}\right)\left(\frac{\nu_p}{\nu_S}\right)^3\left(\frac{P_{\mathrm{in}}}{h\Delta\nu_S^{(f)}\Delta\nu_p^{(f)}}\right)\left(Nc\frac{\mathrm{d}\sigma}{\mathrm{d}\Omega}\right). \tag{11}$$

Here NA is the numerical aperture of a lens (where $d/f = 2\mathrm{NA}$, typically NA = $0.002 \rightarrow 1$). For a Stokes emission frequency and wavenumber line-width of $\nu_S = 4.9 \times 10^{14}$ Hz and $\Delta\tilde{\nu}_S = 10\ \mathrm{cm}^{-1}$ (encapsulating many linewidths from the individual Q-branches), respectively, the free space Stokes line-width in frequency space can be expected to be $\Delta\nu_S^{(f)} = 3.0 \times 10^{11}$ Hz [45,46]. For a pump frequency and line-width of $\nu_p = 5.6 \times 10^{14}$ Hz and $\Delta\nu_p^{(f)} = 5.0 \times 10^9$ Hz [47], respectively, the following assumptions can also be applied: $\nu_p/\nu_S \approx 1$, $\Delta\nu_S = \Delta\nu_S^{(f)} > \Delta\nu_p^{(f)}$ and $n = 1$, resulting in the following equation:

$$\gamma_f = \left(\frac{3\mathrm{NA}^3}{16}\right)\left(\frac{P_{\mathrm{in}}}{h\Delta\nu_S^2}\right)\left(Nc\frac{\mathrm{d}\sigma}{\mathrm{d}\Omega}\right). \tag{12}$$

The simplified scaled rate of emission per molecule in free space is then given by

$$\frac{\gamma_f}{Nc\frac{\mathrm{d}\sigma}{\mathrm{d}\Omega}} = \left(\frac{3\mathrm{NA}^3}{16}\right)\left(\frac{P_{\mathrm{in}}}{h\Delta\nu_S^2}\right). \tag{13}$$

For an optical setup with NA = 0.003 ($d = 0.003$ m and $f = 0.5$ m) and a laser power of 200 mW, the scaled rate of emission per molecule in free space is on the order of 1500 (using Eq. 11). The maximum scaled rate of emission can be expected for a large diameter high power laser beam with a narrow line-width focused with a short focal length lens. Note that a limit is reached for a diffraction limited spot (NA = 1). However, the practical constraints on NA values in *in situ* measurements mean large values of NA are not attainable, so that alternative solutions must be found. Next we discuss the experimental arrangement used to measure the Stokes photons for atmospheric free space measurements.

2.3. Free space setup

Figure 2 shows the experimental setup used to carry out the free space measurements. The pump radiation is provided by a green/blue argon-ion laser (Spectra Physics Stabilite 2017). The laser beam output gives nine output wavelengths with two intense lines at 514.5 nm (maximum 2 W) and 488.0 nm (maximum 1.5 W). Changing the current allows for the power output of each line to vary between 0 W and the maximum value. The delivered maximum laser power was lower than 2 W (at 514.5 nm) due losses in the fiber guiding the light onto the are of interest. Dichroic filters are then used to separate out the blue and green lines before a 50 mm diameter lens ($f = 0.5$ m), coated for the visible wavelengths, focuses the 514.5 nm beam ($d = 3$ mm) to a spot with diameter of approximately 110 μm. The power output of 514.5 nm was measured to be 200 mW at the focus.

Both Rayleigh and Stokes photons are collected by a 90° lens setup. Firstly a 50 mm diameter lens with 0.1 m focal length collimates the photons, followed by a second 50 mm diameter lens with 0.1 m focal length, which focuses the light onto a 1000 μm fiber. The fiber output is collimated using a 50 mm diameter lens with a 0.1 m focal length before passing through a long-pass 532 nm dichroic filter (LPD02-532RU-25). The transmitted Stokes photons are then focused down by a lens with 0.1 m focal length onto the aperture of an Andor Shamrock SR-303i spectrograph with a slit size of 150 μm, which uses a 600 l/mm grating prism. The output of the spectrograph is monitored by an Andor Ixon Ultra-888 EM-CCD camera. The spectrograph and

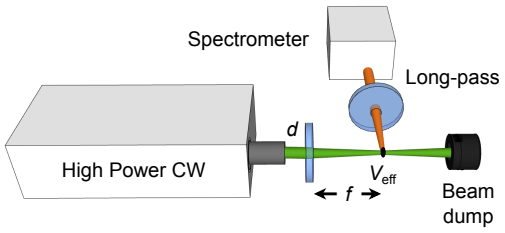

Fig. 2. Experimental setup for free space gas-phase Raman detection with a CW laser.

the EM-CCD are an integrated system, with electron multiplying capabilities, as the expected Raman signals are usually weak. Next, we discuss the potential enhancement of spontaneous Raman scattering within an optical cavity.

3. Cavity enhanced Raman scattering

3.1. Conditions for efficient resonant cavity enhancement

The optimal performance of resonant cavities requires that the light has to be both geometrically and phase coupled into the cavity. The following subsections below describe the geometric conditions required for mode matching, and the resulting emission rate at the matched conditions.

3.1.1. Mode matching

A typical solid state or gas phase laser consists of a resonant cavity containing an excited medium. This results in laser emission with a characteristic beam waist and divergence angle. In order to achieve effective coupling of light into an external cavity, the laser beam needs to be shaped by appropriate optics in such a way that it retraces the contours of said cavity's $\mathrm{TEM}_{0,0}$ mode. This suppresses higher order modes, ensuring that the resonant recirculation (see Section 3.3) occurs across the same spatial and phase location, resulting in power build-up. This is realized by organizing mirrors placed an integer multiple of the incident half-wavelength away from each other.

In order to achieve effective mode matching, two beam waists (cavity and laser) need to be well overlapped. For a cavity consisting of two spherical mirrors with equal radii of curvature ($\mathcal{R}$) the beam radius w_0 at the centre of the cavity is given by [48]:

$$\left(\frac{w_0}{l}\right)^2 = \frac{\lambda_p}{l}\frac{1}{2\pi}\sqrt{2\frac{\mathcal{R}}{l}-1}\,, \tag{14}$$

where l is the length of the cavity. In order to mode match the laser beam into the cavity one has to choose a lens which has a focal length larger than the characteristic length f_0 given by [49]:

$$f_0 = \frac{\pi w_0 w_1}{\lambda_p}\,, \tag{15}$$

where w_1 is the Gaussian laser beam radius. Therefore, any lens with a focal length $f > f_0$ can be used to mode match. Once the appropriate focal length has been established, the lens needs to be placed at a set distance from the laser and cavity beam radii in order to overlap the beams (see Figure 3 (a)). The lens-cavity beam radius distance d_0 and the laser beam-lens distance d_1 are calculated by the following equations [50]:

$$d_0 = f \pm \frac{w_0}{w_1}\sqrt{f^2 - f_0^2} \qquad \text{and} \qquad d_1 = f \pm \frac{w_1}{w_0}\sqrt{f^2 - f_0^2}\,. \tag{16}$$

Table 2. Parameters inside an optical cavity of length l = 3 mm with mirrors of equal radii of curvature $\mathcal{R}$ = 1 m and fringe-spacing integer Q = 10.

λ (nm)	R_1	R_2	T_1	T_2	w_0 (μm)	$\mathcal{F}_R$	$\mathcal{F}_{p/S}$
532	0.999	0.99993	0.001	0.00007	81	5870	4000
607	0.4	0.4	0.6	0.6	86	3.3	3.3

Figure 3 (a) shows the mode parameters of $TEM_{0,0}$ inside an optical cavity with mirrors of equal radii of curvature and the matching condition for two $TEM_{0,0}$ modes using a thin lens. The equations for more complicated beam waist geometries can be found in a review paper [48].

3.1.2. Finesse

The purpose of a cavity is to isolate and build up the power over a small number of modes. Under the assumption that all higher order modes are distinguished the quantity that describes its effectiveness is called finesse, $\mathcal{F}$ [51]:

$$\mathcal{F} = \frac{\Delta\nu_{\mathrm{FSR}}}{\Delta\nu^{(c)}} \tag{17}$$

where $\Delta\nu_{\mathrm{FSR}} = \frac{c}{2nl}$ is the free spectral range corresponding to the axial displacement of the modes in the cavity, and $\Delta\nu^{(c)}$ is the actual spectral width obtainable in the cavity. Higher finesse values correspond to a finer frequency resolution and thus higher specific power build up. The finesse value is determined by the cavity's losses, which arise from the mirror reflectivities at the particular wavelength, an interference factor which depends on the geometry of the mirrors and the wavelength used, as well as the estimated surface quality of the mirrors. The reflectivity finesse corresponding to monochromatic light is given by [52]:

$$\mathcal{F}_R = \frac{\pi(R_1R_2)^{(1/4)}}{1-\sqrt{R_1R_2}} \tag{18}$$

where R_1 and R_2 are the reflectivities of the in and out-coupling mirrors, respectively. This expression is applicable for plane, parallel mirrors with a perfect surface quality.

For non-planar mirrors, a second factor, $\mathcal{F}_I$, needs to be considered to account for the radius of curvature. It is given by $\mathcal{F}_I = 16\lambda_{p/S}l^3/H^4$ where H is the beam radius at the in-coupling mirror, defined as

$$\left(\frac{H}{w_0}\right)^2 = 1 + \left(\frac{\lambda_p l}{2\pi w_0^2}\right)^2 = 1 + \frac{1}{2\frac{\mathcal{R}}{l}-1}\ . \tag{19}$$

Finally, the surface quality finesse $\mathcal{F}_Q$, is a measure of the flatness of the mirror's surface, which is usually flat to within a fraction of the wavelength λ/Q, where Q is the fringe-spacing integer, commonly used as a metric for the flatness of the optical surface. This means that no point on the ideal plane deviates by more than λ/Q, therefore it is assumed that $\mathcal{F}_Q = Q/\lambda$. For mirrors with high reflectivites the $\mathcal{F}_Q$ value is usually very large and therefore can be ignored.

Combining all three factors gives a total theoretical finesse of the cavity, $\mathcal{F}$, for a wavelength λ, equals [53]:

$$\frac{1}{\mathcal{F}} = \sqrt{\left(\frac{1}{\mathcal{F}_R}\right)^2 + \left(\frac{1}{\mathcal{F}_Q}\right)^2 + \left(\frac{1}{\mathcal{F}_I}\right)^2} = \sqrt{\left(\frac{1-\sqrt{R_1R_2}}{\pi(R_1R_2)^{(1/4)}}\right)^2 + \left(\frac{\lambda}{Q}\right)^2 + \left(\left(\frac{H}{l}\right)^4\frac{l}{16\lambda}\right)^2}\ . \tag{20}$$

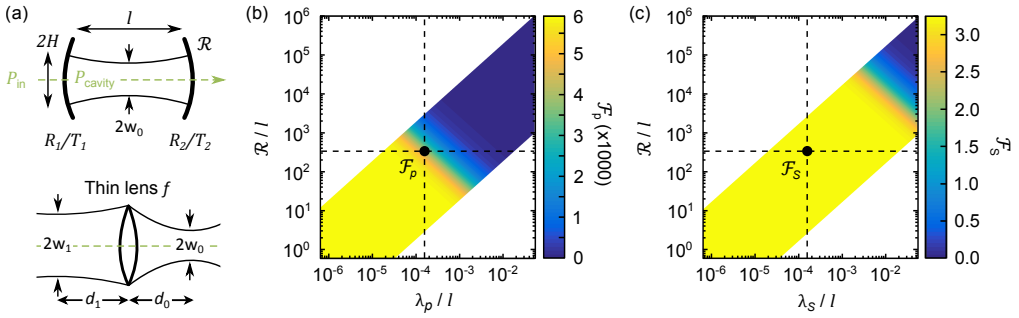

Fig. 3. (a) Schematics of the parameters required for efficient resonant cavity enhancement. Colourmaps (b) and (c) show the calculated pump and Stokes emission finesse (Eq. 20) as a function of nondimensional parameters: $\mathcal{R}/l$ and $\lambda_{p/S}/l$, respectively. Dashed lines indicate the location of experimental values of nondimensional parameter ratios in the present work. The white regions within the maps correspond to finesse values for unrealizable configurations.

Figure 3 (b) and (c) show the calculated finesse values (using Eq. 20) for the pump and Stokes emission wavelengths, respectively, as a function of the nondimensional parameters $\mathcal{R}/l$ and λ/l. The figure illustrates that in the yellow region, $\mathcal{F}_R$ dominates (*i.e.* $\lambda/l << 1$) and the highest finesse values are dominated by the wavelength specific reflectivity values of both mirrors. In the limit for small cavities, where $\mathcal{F}_I$ dominates (i.e. $\mathcal{R}/l \to \infty$) the finesse is at a minimum, and the value is determined by the length of the cavity. Table 2 gives the wavelength dependent in and out-coupling mirror reflectivities, $R_{1/2}$ and transmissivities, $T_{1/2}$, along with the length of the cavity, l, radii of curvature, $\mathcal{R}$, and fringe-spacing integer, Q. The corresponding calculated (using Eq. 20) finesse values $\mathcal{F}_p$ and $\mathcal{F}_S$ for the pump and Stokes wavelengths, respectively, are also shown.

The measured finesse can be significantly lower than the theoretical values predicted by Eq. 18 using the ideal reflectivity, especially for smaller cavities. In summary, larger cavities can yield higher finesse *if* the mirrors can be appropriately positioned. However, it is often the case that it is in practice difficult to control the exact positioning of the mirrors, so that it is easier to obtain a power build-up in a cavity of smaller length, which offers larger $\Delta\nu_{\mathrm{FSR}} = c/(2nl)$, allowing easier stabilization of a smaller number of modes with limited control accuracy.

3.1.3. Impedance matching

In order to achieve a large power build up inside the cavity its mirrors must have high reflectivity values. This could lead to difficulties in injecting the pump beam into the cavity, as major losses could occur due to the initial back reflection from the in-coupling mirror (see Figure 5 (b)). In order to minimize such losses the optical cavity must be impedance-matched [54, 55]. To achieve this, the transmission coefficient of the in-coupling mirror for the pump radiation wavelength must be equal to all the other losses occurring inside the cavity, mathematically given by:

$$T_1 = T_2 + A \tag{21}$$

where T_1 and T_2 are the transmission coefficients of the in- and out-coupling mirrors, respectively, and A represents the total losses of the cavity. Therefore, when the transmissivity of the input mirror is larger (smaller) than that of the addition of the transmissivity of the output mirror and the loss coefficient, the system is said to be over (under) coupled.

In reality, it can be difficult to determine upfront the exact losses within the resonator for an arbitrary scatterer and it is difficult to dynamically adjust mirror reflectivities. For the cavity

model in Section 3.2 we assume all of the light is getting into the cavity. Therefore, the power in the cavity corresponds to the power measured before entering the in-coupling mirror.

3.1.4. Mode locking

The final condition required for the efficient enhancement is that the cavity length must be correct within a fraction of an optical wavelength. An electronic feedback loop is often used for maintaining the resonance. Such feedback loops may either adjust the optical frequency of the laser to match the cavity frequency, or adjust the cavity length via a piezoelectric actuator. A number of different techniques have been used for locking the cavity into a resonance state [30, 56–58].

A Pound-Drever-Hall lock-in scheme is the more popular of the techniques, which locks the laser frequency to the resonance frequency of the cavity [58] based on a measurement of the phase offset. With proper execution it is able to reduce the laser line-width and stabilize the frequency drifts to a particular cavity mode. Hippler *et al.* used an alternative technique by building a low cost lock-in amplifier, which adjusts the cavity length via a piezo-actuator [57]. For this work we decided to use the low cost lock-in device which is able to achieve lock-in, but suffers from long time scale drift. This technique was chosen due to the cost and ease of use. In their most recent work, Hippler *et. al.* [56] have achieved lock-in using the optical transmission of the cavity and found that the laser can effectively self-lock without the need for an additional electronic feedback. However this requires a Fabry-Perot laser diode unlike the 532 nm DPSS laser diode used in the current work.

3.2. Cavity model

The rate of change in photons emitted in a cavity is given by a balance between the emission induced by the rate of pumping photons to the flux of photons emitted in the cavity [42, 43].

$$\frac{\mathrm{d}n_S}{\mathrm{d}t} = \frac{C_c}{\tau_0} n_p - \frac{1}{\tau_c} n_S \,, \tag{22}$$

where τ_0 and τ_c are the lifetimes of the Stokes photons in free space and in the cavity, respectively. In the regime where the cavity mode is much narrower than the Stokes mode [59] the effective cavity Purcell factor, C_c, is given by

$$C_c = \frac{3}{4\pi^2} \left(\frac{\lambda_S}{n}\right)^3 \frac{1}{V_{\mathrm{eff}}^{(c)}} \frac{\nu_S}{\Delta\nu_S^{(f)} + \Delta\nu_S^{(c)}} \,, \tag{23}$$

where $\Delta\nu_S^{(f)}$ and $\Delta\nu_S^{(c)}$ are the free space and cavity Stokes linewidths and $V_{\mathrm{eff}}^{(c)}$ is the effective mode volume given by [42, 48]

$$V_{\mathrm{eff}}^{(c)} = \frac{(\lambda_p + \lambda_S) l^2}{4 \tan^{-1}(1/\sqrt{2\mathcal{R}/l - 1})} \,, \tag{24}$$

By assuming a steady state solution ($\mathrm{d}n_s/\mathrm{d}t = 0$) and solving for the rate of the emission of Stokes photons leaving the cavity ($\gamma_c = n_S/\tau_c$), Eq. 22 becomes

$$\gamma_c = \left(\frac{8Nc^3}{\pi l^2 n^3} \frac{\mathrm{d}\sigma}{\mathrm{d}\Omega} \frac{\nu_p^2}{\nu_S^2(\nu_p + \nu_S)} \frac{1}{\Delta\nu_S^{(f)} + \Delta\nu_S^{(c)}} \tan^{-1}\left(\frac{1}{\sqrt{2\mathcal{R}/l - 1}} \right) \right) n_p \,. \tag{25}$$

Here it is assumed as before that the incoming power is distributed uniformly over the pump wavelength, $n_p = 2P_{\mathrm{in}}\tau_p^{(c)}/h\nu_p$ where P_{in} is the pump input power and $\tau_p^{(c)} = 1/(2\pi\Delta\nu_p^{(c)})$, where $\Delta\nu_p^{(c)}$ is the cavity pump line-width. The values for $\Delta\nu_p^{(c)}$ and $\Delta\nu_S^{(c)}$ are expressed as a function

of the free spectral range and finesse at the respective frequency given by Eq.17. The larger the finesse and length the smaller the respective linewidths will be. A factor of 1/2 is also introduced into the overall Eq. 25 to account for the fact that light is collected from only one side of the cavity. The final expression for the rate of emission from one side of the cavity is

$$\gamma_c = \frac{4\beta c^3 P_{\text{in}} N}{h\pi^2 l^2 n^3} \frac{\mathrm{d}\sigma}{\mathrm{d}\Omega} \frac{\nu_p}{\nu_S^2(\nu_p + \nu_S)} \frac{1}{\frac{c}{2nl\mathcal{F}_p}\left(\Delta\nu_S^{(f)} + \frac{c}{2nl\mathcal{F}_S}\right)}, \tag{26}$$

where $\beta = \tan^{-1}(1/\sqrt{2\mathcal{R}/l - 1})$. The equation can be regrouped to yield a similar expression as the total photon emission in the free case.

$$\gamma_c = \left(\frac{8\mathcal{F}_p\beta}{\pi^2 n^2}\right)\left(\frac{\nu_p}{\nu_S}\right)\left(\frac{P_{\text{in}}}{h\nu_S(\Delta\nu_S^{(f)} + \frac{c}{2nl\mathcal{F}_S})}\right)\left(\frac{c}{l(\nu_p + \nu_S)}\right)\left(Nc\frac{\mathrm{d}\sigma}{\mathrm{d}\Omega}\right). \tag{27}$$

We can glean insight into the relative contributions for the cavity mode by considering the order of magnitude of the groupings for the current conditions. Stokes emission frequency and line-width are $\nu_S = 4.9 \times 10^{14}$ Hz and $\Delta\nu_S^{(f)} = 3.0 \times 10^{11}$ Hz, respectively. The pump frequency and line-width are $\nu_p = 5.6 \times 10^{14}$ Hz and $\Delta\nu_p^{(f)} = 5.0 \times 10^{9}$ Hz, respectively. In addition, $\mathcal{F}_p = 4000$ and $\mathcal{F}_S = 3$ (see Table 2). To simplify this expression further we can now make the following assumptions: $\nu_p/\nu_S \approx 1$, $\Delta\nu_S = \Delta\nu_S^{(f)} >> c/2nl\mathcal{F}_S$ and $n = 1$ to give

$$\gamma_c = \left(\frac{4\mathcal{F}_p\beta}{\pi^2}\right)\left(\frac{P_{\text{in}}}{h\nu_S\Delta\nu_S}\right)\left(\frac{c}{l\nu_S}\right)\left(Nc\frac{\mathrm{d}\sigma}{\mathrm{d}\Omega}\right). \tag{28}$$

Resulting in a simplified scaled rate of emission per molecule in a cavity, given by

$$\frac{\gamma_c}{Nc\frac{\mathrm{d}\sigma}{\mathrm{d}\Omega}} = \left(\frac{4\mathcal{F}_p\beta}{\pi^2}\right)\left(\frac{P_{\text{in}}}{h\nu_S\Delta\nu_S}\right)\left(\frac{c}{l\nu_S}\right). \tag{29}$$

For instance, with a cavity setup of $l = 3$ mm, $\mathcal{R} = 1$ m and a laser power of 20 mW, the scaled rate of emission per molecule in a cavity is on the order of 2800 (using Eq. 27). Note this value is approximately 2 times larger than in the free space case calculated in Section 2.2, where the same pump line-width was used but for an order of magnitude more pump power (200 mW instead of 20 mW). The maximum scaled rate of emission can be expected for a high power laser beam with a narrow line-width focused into a short cavity with a high finesse. Next we discuss in detail about the three factors that have contributed to the enhancement of spontaneous Raman scattering within an optical cavity.

3.3. Resonant recirculation, Purcell effect and double resonance condition

The enhancement of spontaneous Raman scattering in a cavity is attributed to resonant recirculation, the Purcell effect and double resonance condition. Figure 4 shows the three main factors (resonant recirculation, Purcell effect and double resonance condition) that contribute to the enhancement of spontaneous Raman scattering in a cavity. For light to be efficiently coupled into a cavity recirculation requires that the laser and the cavity frequencies are resonant with each other. The power build up within the cavity is proportional to the finesse ($P_{\text{cavity}} \propto \mathcal{F}_p\, P_{\text{in}}$, see Eq. 17 and Eq. 27), as it represents the ratio of the power contained per unit mode of the the cavity. For instance, for an incident laser with a power of 20 mW and a cavity with finesse of value around 4000 (see Section 3.1) one can expect recirculation powers on the order of tens of watts. Such enhanced powers create proportionally more Raman scattered photons that can be detected for the low cross sections of gas molecules of interest, whilst demanding sufficient precision in rejecting modes away from the selected region.

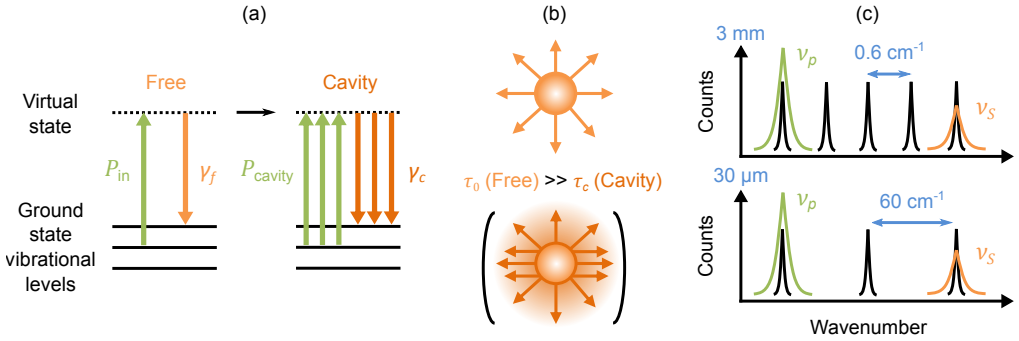

Fig. 4. Three main factors that contribute to the enhancement of spontaneous Raman scattering within a cavity: (a) Resonant recirculation, (b) Purcell effect and (c) Double resonance condition.

The photons emitted in the laser-excited Raman processes have a certain free lifetime, τ_0. However, by introducing an external cavity the rate of this emission can be increased due to the Purcell effect [60] (see Eq.23). The photons emitted for the Stokes modes become confined, causing an increase in the density of states into which the molecule can scatter and, consequently, resulting in a decrease in the lifetime of emission, τ_c.

The double resonance condition states that when the cavity length is set such that the number of Free Spectral Ranges ($\Delta\nu_{\mathrm{FSR}}$) equals the shift of the Raman mode of interest, not only are the incident laser and cavity modes resonant but the scattered light exiting the cavity at the Stokes frequencies are as well. This results in an enhancement of the scattered light exiting the cavity. For the current conditions with a cavity of length 3 mm, $\Delta\nu_{\mathrm{FSR}} \approx 50$ GHz (0.6 cm^{-1}). For a cavity illuminated at $\lambda_p = 532$ nm (5.64×10^5 GHz), the scattered modes are enhanced approximately every 0.02 nm. In the case of the N_2 vibrational mode emitting at a frequency 2331 cm^{-1}, there are over 3900 modes which can be enhanced between the excited frequency and this vibrationally scattered mode. The $\Delta\nu_{FSR}$ for cavities of the order of tens of micrometers however, are of the order of 5000 GHz (60 cm^{-1}) making it very difficult for the scattered Stokes photons to be enhanced, as each enhanced mode is separated by approximately 2 nm. Therefore only 39 modes are enhanced for the example of N_2. Additionally, as the width of the vibrationally scattered mode is approximately 10 cm^{-1}, it would be quite easy for it to be missed with a cavity that provides only 60 cm^{-1} resolution.

As a final note, manufacturing constraints in high reflectivity mirrors of the cavity mirrors must also be taken into account when considering the double resonance condition, as one can normally expect decreasing oscillatory reflectivity behaviour for wavelengths further away from the pump wavelength. An ideal confocal Fabry-Perot cavity would need to be resonant with both the pump and Stokes frequencies in order to utilize all of the three simultaneously occurring processes to give increased number of scattered Stokes photons at a faster rate of emission.

3.4. *Cavity setup*

Figure 5 (a) shows the experimental setup used to carry out the CERS measurements. The pump radiation for CERS is provided by a green CW DJ532-40 Thorlabs solid state laser. The laser diode is assembled in a Thorlabs TCLDM9 Thermo-electrically cooled mount. Control of the diode's current and temperature is enabled by the use of Thorlabs LDC205C and TED200C controllers, respectively, allowing change in the laser output power and wavelength.

Light from the diode laser is collimated with an aspheric lens, after which it goes through a Faraday isolator, which shield against back reflections, preventing the diode from destabilizing. A knife edge technique was used to measure the beam waist radius w_1 of the collimated incoming

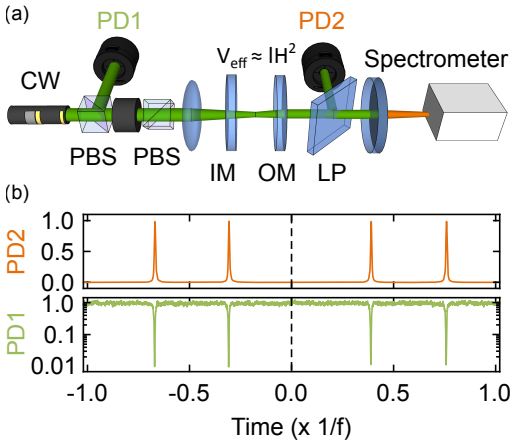

Fig. 5. (a) CERS experimental setup for gas-phase Raman detection. IM = input mirror, OM = output mirror, PD(1/2) = Photodiode (1/2), PBS = Polarizing Beam Splitter, LP = Long-pass filter and CW = Continuous Wave. (b) Normalized voltage signals for modes transmitted through the cavity (PD2 - orange) and modes reflected from the in-coupling mirror (PD1 - green) as a function of the normalised modulation frequency.

radiation to be 500 μm. The collimation was checked by measuring the beam waist w_1 at various points along the beam over a distance of 1.5 m, which was found to be unchanged. For a cavity distance of l = 3 mm and radius of curvature $\mathcal{R}$ = 1 m, the calculated beam radius for the cavity (using Eq. 14) is w_0 = 81 μm at 532 nm.

The characteristic length was calculated (using Eq. 15) to be f_0 = 240 mm using the values of w_1 = 500 μm and w_0 = 81 μm. This means a lens with f = 250 mm was suitable for mode matching. Since the laser beam was collimated, it was only necessary to calculate the distance d_0 (using Eq. 16) to establish the displacement of the lens from the in-coupling mirror, which was determined to be 262 mm. The mode matching lens couples the laser light into a linear optical cavity consisting of two highly reflective in-coupling [61] and out-coupling [62] mirrors, with the reflectivity values for a corresponding wavelength listed in Table 2.

In order to achieve resonance in the cavity and observe signal output, the cavity length needs to be a half-wavelength integer multiple of the lasing wavelength. In reality this condition can be difficult to achieve, so it is common to mount the mirrors onto piezo actuated mounts that possess a nanoscale precision, and to attach these mounts to a translational stage that has micron-scale positioning precision. The kinematic mirror mounts used are Thorlabs Polaris - K1PZ coupled with piezo electric actuators (Polaris Thorlabs MDT693B), which possess three directional axes of control. The translational stage used was Thorlabs PT1B/M. A modulation signal fed into the piezo controllers allows length changes on the order of micrometers. The resonance position of the out-coupling mirror is enforced by driving the piezo actuator using a periodic triangle function (with frequency of 100 Hz) provided by a Wavetek model 142 analog signal generator.

If the system is in resonance, the cavity produces a series of light pulses that are incident on a 532 nm long-pass dichroic mirror (LPD02-532RU-25), which allows the Raman signal to pass through and reflect the pump laser radiation at 90°. The reflected pump radiation is focused onto a Thorlabs photomultiplier PMM01 (PD2) via a f = 50 mm lens. The signal read by PMM01 is then used in a feedback circuit to minimize the magnitude of higher order TEM modes via cavity alignment. Figure 5 (b) shows the PMM01 signal observed during the periodic displacement of the output mirror, with the experimental finesse being determined by the magnitude of the cavity line-widths and calculated $\Delta\nu_{\mathrm{FSR}}$. The authors chose a forward collection geometry instead of the 90° collection geometry from the center of the cavity as they can benefit from not only the

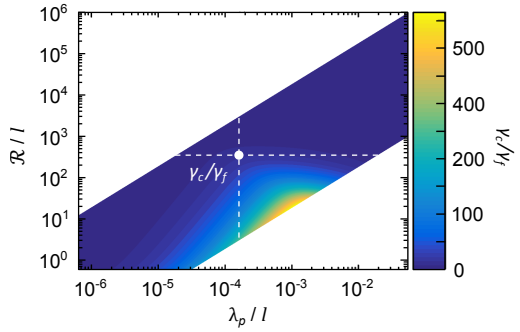

Fig. 6. Theoretical ratio of CERS vs. free space Stokes photon emission rate ratio for N_2 in air, as a function of nondimensional parameters: $\mathcal{R}/l$ and λ_p/l. The dashed white lines indicate experimental values of nondimensional parameter ratios. The Stokes photon emission ratio was calculated by using Eq. 30 with a NA value of 0.003, corresponding experimental values.

increased effective volume but also from any small increases in signal due to the Purcell effect.

Additionally, during the periodic length modulation, the light reflected from the in-coupling mirror is collected at the exit of the Faraday isolator and is focused down onto a Thorlabs photodiode DET10A (PD1) via a f = 50 mm lens. This signal provides information on the impedance matching for the optical cavity. Figure 5 (b) also shows the reflected signal from the in-coupling mirror to highlight the fraction of light getting into the cavity on resonance. In order to estimate the absorption losses in the resonator, Eq. 21 was used with the reflectivity values of the cavity mirrors at 532 nm shown in Table 2. The absorption losses, A, were determined to be 9.3×10^{-4} (using Eq. 21) for an impedance-matched cavity. In reality, the cavity is likely to be over coupled as a result of the higher transmission coefficient of the in-coupling mirror. Therefore, the cavity benefits from larger recirculation power due to the increased transmission. Yet the cavity also suffers from lower excitation power transmitted due to the lower transmission coefficient of the out-coupling mirror [54].

Once the cavity has been successfully aligned, the piezo modulation signal gets changed to a rising DC offset until resonance is achieved and PMM01 detects a mode output. The PMM01 signal is fed into the lock-in amplifier that is sensitive to the voltage changes in the cavity signal. The out-coupling mirror position is corrected by the lock-in amplifier via a feedback DC voltage signal fed into the signal generator, which in turn alters its DC signal in order to bring the out-coupling mirror back to the resonance position, resulting in a cavity behaving as a high power CW laser.

The radiation that passes through the dichroic mirror consists of Stokes signal, as the anti-Stokes signals are below 532 nm and are blocked by the long-pass dichroic mirror (LPD02-532RU-25). Similarly to the CW setup, the Stokes photons are focused down by a lens of f = 100 mm onto the aperture of the Andor Shamrock SR-303i spectrograph with a slit size of 150 μm, which uses a 600 l/mm grating prism. The output of the spectrograph is monitored by the Andor Ixon Ultra-888 EM-CCD camera. The spectrograph and the EM-CCD are an integrated system, with electron multiplying capabilities as the expected Raman signals are usually weak. Now that we have discussed both the models and the experimental procedures for free space and cavity based methods, next we compare and discuss the ratios we calculate and measure for room air.

4. Comparison of free space and cavity methods

4.1. Model comparison

To obtain the ratio of theoretical signal for experiments with and without cavity amplification we now divide Eq. 27 by Eq. 11, resulting in:

$$\frac{\gamma_c}{\gamma_f} = \left(\frac{128n}{3\pi^2}\frac{1}{\mathrm{NA}^3}\mathcal{F}_p\beta\right)\left(\frac{\nu_S}{\nu_p}\right)^2\left(\frac{\Delta\nu_S^{(f)}}{\Delta\nu_S^{(f)} + \frac{c}{2nl\mathcal{F}_S}}\right)\left(\frac{c\Delta\nu_p^{(f)}}{\nu_S l(\nu_p + \nu_S)}\right)\left(\frac{P_c N_c}{P_f N_f}\right). \tag{30}$$

where $P_{c/f}$ and $N_{c/f}$ are the input power and molecular number density for the free space and cavity-based methods, respectively. In order to find the main parameters governing the gain for a high power CW laser in free space compared to the same laser coupled with a high finesse cavity, we make the assumptions that the same laser power and sample conditions are used, so that $P_c N_c = P_f N_f$. We also assume that $\nu_S/\nu_p \approx 1$, and that for cases with macroscopic cavities, $c/(2nl\mathcal{F}_S) < \Delta\nu_S^{(f)} = \Delta\nu_S$ and $n = 1$. We also know that $\Delta\nu_p^{(f)} = c\Delta\lambda_p^{(f)}/\lambda_p^2$. We substitute ε as the relative line width for the laser used, so that $\Delta\lambda_p^{(f)} = \Delta\lambda_p = \varepsilon\lambda_p$, with a value $\varepsilon \approx 1 \times 10^{-5}$ in this work, and the simplified expression for the ratio becomes:

$$\frac{\gamma_c}{\gamma_f} = \left(\frac{64\varepsilon}{3\pi^2}\frac{1}{\mathrm{NA}^3}\,\mathcal{F}_p(\lambda_p/l, \mathcal{R}/l)\,\beta(\mathcal{R}/l)\right)\left(\frac{\lambda_p}{l}\right). \tag{31}$$

Equation 31 shows that the main factor controlling the amplification is NA, as that represents the total effective volume in free space. The larger the volume illuminated with the same power, the larger the signal obtained in free space, and thus the smaller the relative amplification obtained by a cavity setup. Values for the ratio in Eq. 31 are plotted in Figure 6 using a value of NA = 0.003, which is consistent with the parameters used in the present experiments. However, for realistic ranges between around NA = 0.002 $\rightarrow$ 1, the maximum Stokes emission ratio magnitudes could range from 10^{-2} to 10^4.

Figure 6 shows that for a fixed pump wavelength, higher emission values using a cavity are obtained for either smaller cavities, or smaller radius of curvature. To achieve the highest γ_c/γ_f ratio for an excitation wavelength of 532 nm, the ideal cavity length and radius of curvature are ≈ 50 μm and ≈ 10 cm, respectively. Please note that, as discussed in Section 3.3, as the length of the cavity is reduced, the number of possible modes within the cavity also decreases. The resonant emission will occur every several nanometers (for a μm cavity) rather than a fraction of a nanometer (for a mm cavity), giving a greatly reduced emission spectrum (see Figure 4 (c)) due to difficulty in meeting the double resonance condition.

The value for $\mathcal{F}_S$ (in Eq. 30) used in our experiments is limited to 3 due to the values of the mirror reflectivities at the Stokes wavelength, which is substantially smaller than the pump finesse, $\mathcal{F}_p$ which is closer to 4000. Therefore, $\mathcal{F}_p$, and the resonant recirculation process dominates the γ_c/γ_f ratio as shown in Eq. 31. It is possible to further increase the ratio value by ensuring that the correct optical elements for the species of interest are used in order to increase the value of $\mathcal{F}_S$. In general this value will very much depend on the mirrors used and the Stokes wavelength. For an increased reflectivity at the Stokes wavelength, the influence of the Purcell effect on the γ_c/γ_f ratio can be explored. In this regime the assumption that $c/2nl\mathcal{F}_S < \Delta\nu_S^{(f)}$ no longer holds true and $\mathcal{F}_S$ becomes important. Similarly to the $\mathcal{F}_p$, $\mathcal{F}_S$ also depends on the parameters $\mathcal{R}/l$ and λ_S/l. Therefore when the Purcell effect has a significant contribution the expected γ_c/γ_f ratio will have a more complex dependence. In order to distinguish between the contributions from the recirculating power and Purcell effect, one would have to measure the flux of Stokes photons in the forward scattering geometry along with the 90° scattering geometry from the middle of the cavity. Accounting for the differences in effective volume, any measured increase in the flux of Stokes photons would be due to the Purcell effect.

Table 3. Parameters used for acquisition of theoretical and experimental ratios for a N_2 molecule in CERS and CW techniques. EM gain = 200 and integration time = 60 s for both methods.

Experiment type	CERS	CW	Ratio
P_{in} (W)	0.02 (P_c)	0.2 (P_f)	0.1
NA	-	0.003	-
l (m)	0.003	-	-
$\mathcal{R}$ (m)	1	-	-
Theoretical (photons s^{-1})	611 (γ_c)	335 (γ_f)	1.8
Experimental signal ($\times 10^5$ counts)	27	8.8	3.1

Figure 6 shows that the theoretical value of γ_c/γ_f for the present investigation should be around 18 for the same total input power. In order to compare the effectiveness of the CERS to free space technique, we show the expected power dependent Stokes emission values to be γ_f = 335 photons s^{-1} and γ_c = 611 photons s^{-1} by using Eq. 11 and Eq. 28, respectively, in conjunction with their complementary input parameters shown in Table 3. Next we discuss the two species (N_2 and O_2) of interest and compare the experimentally measured normalized signals in respect to these predicted values.

4.2. Experimental comparison

Figure 7 shows the CW and CERS acquired Raman spectra for laboratory air, with the corresponding N_2 and O_2 peaks appearing at their respective 2331 cm^{-1} and 1555 cm^{-1} Raman shift values. To recall, the differential Raman scattering cross section values for N_2 and O_2 are listed in Table 1 and the experimental parameters are outlined in Table 3. The laser power values outlined in Table 3 were the maximum powers achieved for the respective lasers after they passed through all of the respective optical elements in order to arrive to the sampling area of interest. As can be seen in Figure 7 (a) and Figure 7 (b) the measured count numbers for N_2 integrated over the 2331 cm^{-1} peak areas are approximately 8.8×10^5 counts and 27×10^5 counts for an integration time of 60 s, for CW and CERS, respectively. As the measurements were carried out with an EM gain of 200, the normalized values for the CW and CERS techniques are 73 counts s^{-1} and 225 counts s^{-1} (assuming linear gain), respectively.

Naively one could also compare the measured counts s^{-1} with the theoretically determined photons s^{-1} calculated in Section 4.1. The discrepancies between the theoretical and experimental values are shown in Table 3. For the CW case these differences could be accredited to the imperfections in the size and the overlap between the collection and illuminated volumes, which are assumed to be ideal in Eq. 8. Additionally, there are optical losses through the coupling optical fibre, resulting in not all of the generated Stokes photons being transmitted through the collection optics. Furthermore, the theoretical number was calculated for a pump wavelength of 532 nm, whereas the radiation source used was centred at 514.5 nm. This leads to one expecting a larger differential Raman cross section for a lower wavelength, which would result in more photons. The decision to use the 532 nm pump wavelength for the theoretical calculations was made in order to facilitate the direct comparison between the two employed techniques.

For the CERS case it can be observed in Figure 7 that the line-widths for CERS measurements are approximately twice as wide as the line-widths for the CW measurements. This could be due to multiple modes being excited within the cavity at once, leading to the broadening of the

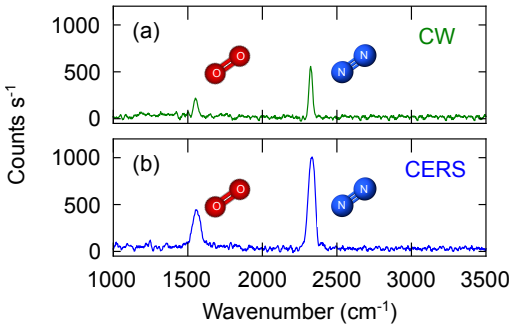

Fig. 7. Spectra of gas-phase Raman detection using (a) CW laser and (b) CERS of room air.

line-width. Furthermore, the stability of the locking technique used in this work was not ideal. It permitted drifts of cavity length over the duration of the experiment for longer exposure times, resulting in a fractional change in the amplified wavelength value, which once again, would lead to the increase of the cavity line-width. In addition, similar to the CW case, it is possible that some of the radiation was lost due to going through additional optical elements before reaching the spectrometer.

In order to compare the theoretical γ_c/γ_f ratio and the experimental ratio, one assumes that the signal scales linearly with power [4] and number density, as stated in Eq. 30. For the free space and cavity based methods the measured power at the focal point was 0.2 W (see Section 2.3) and the measured power before entering the cavity was 0.02 W (see Section 3.4), respectively. In addition, for room air at atmospheric pressure, the number density of oxygen and nitrogen molecules is the same in both the cavity and free space setups. Therefore, hypothetically if the initial laser powers were the same in both experiments ($P_c = P_f$) the experimental ratio would then become 30 rather than 3 (shown in Table 3), which is closer to the model prediction of 18 (calculated by Eq. 30). In order to get a fairer comparison one would need to directly measure the difference between a high power CW laser in free space versus the same laser coupled with a high finesse cavity.

5. Conclusions

In this study we compare the use of spontaneous Raman scattering in gases, using either a high power CW laser or a lower power CW laser with a cavity formed of two mirrors with high reflectivity for the pump laser. A model shows that the main design parameters governing the cavity gain relative to an unconfined system are a) the cavity length relative to the mirror radius of curvature, b) the cavity length relative to the wavelength and c) the numerical aperture used for the free system. The amplification factor varies significantly with experimental conditions for both the free space and cavity based methods. Results show, unsurprisingly, that amplification is not effective for unconfined light collection with the lowest numerical aperture. In reality, high numerical apertures are not feasible for *in situ* applications. This paper shows that for low numerical apertures such as those in furnaces or other remotely accessible devices, cavity based methods can become attractive for multiplying the gas phase Raman signal emerging from the effective volume.

The present paper also analyses the potential and trade-offs for the measurement of gases in practical systems and outlines a comprehensive design process for selecting an appropriate pumping wavelength, cavity length, radius of curvature and reflectivities of the mirrors for a significant signal amplification. This allows investigators to understand the enhancement that can be practically obtained for a particular system and target species.

We compare the expected ratio of unconfined and cavity based signals using theoretical and experimental methods. For the experimental comparison the optical system tested with a relatively large cavity and inexpensive components and lasers, a multiplier of a factor of 18 could be achieved by introducing an external cavity at the same power. In the particular system tested, a cavity system was used to amplify the signal with a laser with an order of magnitude lower power than the unconfined system. The expected signal ratio was 1.8 in favour of the cavity, and the measured value was 3.1. Inaccuracies in the estimation of the geometric and other parameters parameters may have contributed to the observed difference.

6. Acknowledgements

Lee Weller and Maxim Kuvshinov are both funded under EPSRC UK Award EP/M015211/1 within the ANAM Initiative. Maxim Kuvshinov also holds an EPSRC DTA account. We thank Fiona Smail and Jenna Foale (University of Cambridge, Engineering Department) for reading and commenting on the manuscript.

The dataset associated with this article is available at the following DOI (10.17863/CAM.32482) or from the corresponding author on request.

References

1. A. C. Ferrari, "Raman spectroscopy of graphene and graphite: disorder, electron–phonon coupling, doping and nonadiabatic effects," Solid state communications **143**, 47–57 (2007).
2. P. L. Stiles, J. A. Dieringer, N. C. Shah, and R. P. Van Duyne, "Surface-enhanced raman spectroscopy," Annu. Rev. Anal. Chem. **1**, 601–626 (2008).
3. A. Tao, F. Kim, C. Hess, J. Goldberger, R. He, Y. Sun, Y. Xia, and P. Yang, "Langmuir- blodgett silver nanowire monolayers for molecular sensing using surface-enhanced raman spectroscopy," Nano letters **3**, 1229–1233 (2003).
4. P. Graves and D. Gardiner, *Practical Raman Spectroscopy* (Springer, 1989).
5. D. A. Long, *The Raman Effect* (Wiley,, 2002).
6. A. C. Eckbreth, *Laser diagnostics for combustion temperature and species*, vol. 3 (CRC Press, 1996).
7. M. A. Linne, *Spectroscopic measurement: an introduction to the fundamentals* (Elsevier, 2002).
8. J. Kiefer, T. Seeger, S. Steuer, S. Schorsch, M. Weikl, and A. Leipertz, "Design and characterization of a raman-scattering-based sensor system for temporally resolved gas analysis and its application in a gas turbine power plant," Meas. Sci. Technol. **19**, 085408 (2008).
9. J. Kiefer, "Recent advances in the characterization of gaseous and liquid fuels by vibrational spectroscopy," Energies **8**, 3165–3197 (2015).
10. E. J. Blackie, E. C. Le Ru, and P. G. Etchegoin, "Single-molecule surface-enhanced raman spectroscopy of nonresonant molecules," J. Am. Chem. Soc. **131**, 14466–14472 (2009).
11. S. Hartl, D. Geyer, A. Dreizler, G. Magnotti, R. S. Barlow, and C. Hasse, "Regime identification from raman/rayleigh line measurements in partially premixed flames," Combust. Flame **189**, 126–141 (2018).
12. F. Fuest, R. S. Barlow, G. Magnotti, and J. A. Sutton, "Scalar dissipation rates in a turbulent partially-premixed dimethyl ether/air jet flame," Combust. Flame **188**, 41–65 (2018).
13. R. Aroca, *Surface-enhanced vibrational spectroscopy* (John Wiley & Sons, 2006).
14. V. Bergmann, W. Meier, D. Wolff, and W. Stricker, "Application of spontaneous raman and rayleigh scattering and 2d lif for the characterization of a turbulent ch4/h2/n2 jet diffusion flame," Appl. Phys. B **66**, 489–502 (1998).
15. H. Ajrouche, A. Lo, P. Vervisch, and A. Cessou, "1d single-shot thermometry in flames by spontaneous raman scattering through a fast electro-optical shutter," in *17th Inter. Symp. on Applications of Laser Techniques to Fluid Mechanics Lisbon, Portugal,* (2014), pp. 1–17.
16. X. R. Duan, W. Meier, P. Weigand, and B. Lehmann, "Phase-resolved laser raman scattering and laser doppler velocimetry applied to periodic instabilities in a gas turbine model combustor," Appl. Phys. B **80**, 389–396 (2005).
17. K. Muraoka, K. Uchino, and M. Bowden, "Diagnostics of low-density glow discharge plasmas using thomson scattering," Plasma physics controlled fusion **40**, 1221 (1998).
18. R. Keiner, T. Frosch, T. Massad, S. Trumbore, and J. Popp, "Enhanced raman multigas sensing–a novel tool for control and analysis of 13 co 2 labeling experiments in environmental research," Analyst **139**, 3879–3884 (2014).
19. S. Biedrzycki, "Advanced techniques for gas-phase raman spectroscopy," Ph.D. thesis, University of Pittsburgh (2012).
20. L. Martinsson, P.-E. Bengtsson, M. Aldén, S. Kröll, and J. Bonamy, "A test of different rotational raman linewidth models: Accuracy of rotational coherent anti-stokes raman scattering thermometry in nitrogen from 295 to 1850 k," The J. chemical physics **99**, 2466–2477 (1993).
21. I. E. Wachs, "Raman and ir studies of surface metal oxide species on oxide supports: supported metal oxide catalysts," Catal. Today **27**, 437–455 (1996).

22. A. Tokmakoff, M. Lang, D. Larsen, G. Fleming, V. Chernyak, and S. Mukamel, "Two-dimensional raman spectroscopy of vibrational interactions in liquids," Phys. review letters **79**, 2702 (1997).
23. P. Kukura, D. W. McCamant, S. Yoon, D. B. Wandschneider, and R. A. Mathies, "Structural observation of the primary isomerization in vision with femtosecond-stimulated raman," Science **310**, 1006–1009 (2005).
24. S. Hanf, S. Fischer, H. Hartmann, R. Keiner, S. Trumbore, J. Popp, and T. Frosch, "Online investigation of respiratory quotients in pinus sylvestris and picea abies during drought and shading by means of cavity-enhanced raman multi-gas spectrometry," Analyst **140**, 4473–4481 (2015).
25. T. Jochum, J. C. von Fischer, S. Trumbore, J. Popp, and T. Frosch, "Multigas leakage correction in static environmental chambers using sulfur hexafluoride and raman spectroscopy," Anal. chemistry **87**, 11137–11142 (2015).
26. S. C. Eichmann, J. Kiefer, J. Benz, T. Kempf, A. Leipertz, and T. Seeger, "Determination of gas composition in a biogas plant using a raman-based sensor system," Meas. Sci. Technol. **25**, 075503 (2014).
27. T. Frosch, R. Keiner, B. Michalzik, B. Fischer, and J. Popp, "Investigation of gas exchange processes in peat bog ecosystems by means of innovative raman gas spectroscopy," Anal. chemistry **85**, 1295–1299 (2013).
28. T. Jochum, A. Fastnacht, S. E. Trumbore, J. Popp, and T. Frosch, "Direct raman spectroscopic measurements of biological nitrogen fixation under natural conditions: An analytical approach for studying nitrogenase activity," Anal. chemistry **89**, 1117–1122 (2016).
29. R. Salter, J. Chu, and M. Hippler, "Cavity-enhanced raman spectroscopy with optical feedback cw diode lasers for gas phase analysis and spectroscopy," Analyst **137**, 4669–4676 (2012).
30. J. Thorstensen, K. Haugholt, A. Ferber, K. Bakke, and J. Tschudi, "Low-cost resonant cavity raman gas probe for multi-gas detection," J. Eur. Opt. Soc. publications **9** (2014).
31. K. K. Chow, M. Short, S. Lam, A. McWilliams, and H. Zeng, "A raman cell based on hollow core photonic crystal fiber for human breath analysis," Med. physics **41** (2014).
32. Y. Numata, Y. Shinohara, T. Kitayama, and H. Tanaka, "Rapid and accurate quantitative analysis of fermentation gases by raman spectroscopy," Process. Biochem. **48**, 569–574 (2013).
33. S. V, G. J, W. J, and P. S, "Cavity-enhanced raman spectroscopy for food chain management," Sensors **18**, 709–725 (2018).
34. D. Yang, J. Guo, Q. Liu, Z. Luo, J. Yan, and R. Zheng, "Highly sensitive raman system for dissolved gas analysis in water," Appl. optics **55**, 7744–7748 (2016).
35. D. J. Taylor, M. Glugla, and R.-D. Penzhorn, "Enhanced raman sensitivity using an actively stabilized external resonator," Rev. Sci. Instruments **72**, 1970–1976 (2001).
36. S. Ohara, S. Yamaguchi, M. Endo, K. Nanri, and T. Fujioka, "Performance characteristics of power build-up cavity for raman spectroscopic measurement," Opt. review **10**, 342–345 (2003).
37. X. Li, Y. Xia, L. Zhan, and J. Huang, "Near-confocal cavity-enhanced raman spectroscopy for multitrace-gas detection," Opt. letters **33**, 2143–2145 (2008).
38. A. J. Friss, C. M. Limbach, and A. P. Yalin, "Cavity-enhanced rotational raman scattering in gases using a 20 mw near-infrared fiber laser," Opt. letters **41**, 3193–3196 (2016).
39. R. Thalman, K. J. Zarzana, M. A. Tolbert, and R. Volkamer, "Rayleigh scattering cross-section measurements of nitrogen, argon, oxygen and air," J. Quant. Spectrosc. Radiat. Transf. **147**, 171–177 (2014).
40. W. R. Fenner, H. A. Hyatt, J. M. Kellam, and S. Porto, "Raman cross section of some simple gases," JOSA **63**, 73–77 (1973).
41. W. Bischel and G. Black, "Wavelength dependence of raman scattering cross sections from 200-600 nm," in *AIP Conference proceedings,* vol. 100 (AIP, 1983), pp. 181–187.
42. A. Yariv, "Quantum electronics, 3rd," Edn.(John WieLy & Sons, New York, 1988) p **389** (1989).
43. B. J. Petrak, "Microcavity enhanced raman scattering," Ph.D. thesis (2016).
44. T. Niioka, M. Kono, and J. Sato, "Fundamentals of combustion phenomena," Ohmsha Publi-cation Ltd., Tokyo (2001).
45. K. L. McNesby and J. B. Morris, "Fourier transform raman spectroscopy of nitrogen at high pressures," J. Raman Spectrosc. **26**, 487–490 (1995).
46. L. Rahn and R. E. Palmer, "Studies of nitrogen self-broadening at high temperature with inverse raman spectroscopy," JOSA B **3**, 1164–1169 (1986).
47. A. Corney, *Atomic and laser spectroscopy* (Clarendon Press Oxford, 1978).
48. H. Kogelnik and T. Li, "Laser beams and resonators," Appl. optics **5**, 1550–1567 (1966).
49. G. Francois, F. Librecht, and J. Engelen, "Mode matching with a single thin lens," Appl. optics **10**, 1157–1159 (1971).
50. H. Kogelnik, "Imaging of optical modesâĂŤresonators with internal lenses," Bell Syst. Tech. J. **44**, 455–494 (1965).
51. A. E. Siegman, "Lasers university science books," Mill Val. CA **37**, 208 (1986).
52. N. Ismail, C. C. Kores, D. Geskus, and M. Pollnau, "Fabry-pérot resonator: spectral line shapes, generic and related airy distributions, linewidths, finesses, and performance at low or frequency-dependent reflectivity," Opt. express **24**, 16366–16389 (2016).
53. M. Hercher, "The spherical mirror fabry-perot interferometer," Appl. Opt. **7**, 951–966 (1968).
54. C. Bond, D. Brown, A. Freise, and K. A. Strain, "Interferometer techniques for gravitational-wave detection," Living Rev. Relativ. **19**, 3 (2016).
55. D. S. Rabeling, J. H. Chow, M. B. Gray, and D. E. McClelland, "Experimental demonstration of impedance match

locking and control for coupled resonators," Opt. Express **18**, 9314–9323 (2010).
56. T. W. Smith and M. Hippler, "Cavity-enhanced raman spectroscopy in the biosciences: In situ, multicomponent, and isotope selective gas measurements to study hydrogen production and consumption by escherichia coli," Anal. chemistry **89**, 2147–2154 (2017).
57. S. K. Sengupta, J. M. Farnham, and J. E. Whitten, "A simple low-cost lock-in amplifier for the laboratory," J. chemical education **82**, 1399 (2005).
58. R. Drever, J. L. Hall, F. Kowalski, J. Hough, G. Ford, A. Munley, and H. Ward, "Laser phase and frequency stabilization using an optical resonator," Appl. Phys. B **31**, 97–105 (1983).
59. X. Checoury, Z. Han, M. El Kurdi, and P. Boucaud, "Deterministic measurement of the purcell factor in microcavities through raman emission," Phys. Rev. A **81**, 033832 (2010).
60. E. M. Purcell, "Spontaneous emission probabilities at radio frequencies," in *Confined Electrons and Photons,* (Springer, 1995), pp. 839–839.
61. "https://www.layertec.de/en/shop/datasheet-110650/," (2019).
62. "https://www.layertec.de/en/shop/datasheet-109446/," (2019).